

A Lightweight Recurrent Learning Network for Sustainable Compressed Sensing

Yu Zhou, *Member, IEEE*, Yu Chen, Xiao Zhang, *Member, IEEE*, Pan Lai, Lei Huang, *Senior Member, IEEE* and Jianmin Jiang

Abstract—Recently, deep learning-based compressed sensing (CS) has achieved great success in reducing the sampling and computational cost of sensing systems and improving the reconstruction quality. These approaches, however, largely overlook the issue of the computational cost; they rely on complex structures and task-specific operator designs, resulting in extensive storage and high energy consumption in CS imaging systems. In this paper, we propose a lightweight but effective deep neural network based on recurrent learning to achieve a sustainable CS system; it requires a smaller number of parameters but obtains high-quality reconstructions. Specifically, our proposed network consists of an initial reconstruction sub-network and a residual reconstruction sub-network. While the initial reconstruction sub-network has a hierarchical structure to progressively recover the image, reducing the number of parameters, the residual reconstruction sub-network facilitates recurrent residual feature extraction via recurrent learning to perform both feature fusion and deep reconstructions across different scales. In addition, we also demonstrate that, after the initial reconstruction, feature maps with reduced sizes are sufficient to recover the residual information, and thus we achieved a significant reduction in the amount of memory required. Extensive experiments illustrate that our proposed model can achieve a better reconstruction quality than existing state-of-the-art CS algorithms, and it also has a smaller number of network parameters than these algorithms. Our source codes are available at: <https://github.com/C66YU/CSRN>.

Index Terms—Compressed sensing, lightweight neural network, energy efficient, recurrent learning

I. INTRODUCTION

COMPRESSED sensing (CS) theory [1] is an emerging paradigm for signal sampling and reconstruction that demonstrates that sparse signals can be recovered from linear random measurements with a high probability at sample ratios lower than that required by Nyquist sampling theory. In traditional signal processing methods, to make data storage and transmission more convenient, the sampled signal will be

further compressed, with part of the data discarded, resulting in the waste of sampling resources. On the contrary, compressed sensing has the advantage of being able to compress and sample signals simultaneously, which greatly reduces the sampling and computational cost of the sensing system. Therefore, compressed sensing has attracted great attention and been widely used in many applications, such as imaging systems [2], medical scanners [3], etc.

Due to the high efficiency and the many potential applications of CS theory, many algorithms that exploit the potential of compressed sensing for images, such as those reported in [4]–[10], have been explored in the literature. Although these algorithms can recover the original signal well, their common weakness is that all these algorithms attempt to solve convex optimization problems in an iterative manner even though the iterative process is often computationally intensive and thus slows down the reconstruction speed, which limits the real-time performance and further application of these algorithms.

In recent years, deep learning has achieved great success in a range of computer vision tasks due to its advanced performance and high-speed inference abilities; these tasks include image classification [11], super resolution [12] and image restoration [13]. Hence, some CS algorithms based on deep learning have also been proposed [14]–[16]. Compared with traditional CS algorithms, deep learning-based CS algorithms reconstruct images faster thanks to their non-iterative nature. Deep learning-based algorithms take a significant amount of time to learn appropriate model parameters during the training process, but when inferences are being made, the original signal can easily be recovered through computationally efficient matrix multiplications and nonlinear operations. Additionally, the strong learning ability of deep neural networks also ensures that such algorithms can capture the characteristics of signals and provide a better reconstruction quality.

Despite the positive progress that has been achieved, existing deep learning-based CS algorithms still have limitations. On the one hand, current approaches do not fully explore and utilize the the potential power of feature extraction and learning in neural networks, which results in limited reconstruction quality improvement. On the other hand, to achieve high-quality reconstructions, most current methods employ very complex network structures with problem-specific operators, leading to a huge number of parameters to be optimized and extensive memory and energy costs, which impede the use of such algorithms on devices with limited computational resources; these methods cannot meet the demand for sustainable artificial intelligence in our modern society. It is worth

This work was supported in part by the Natural Science Foundation China (NSFC) for Distinguished Young Scholars under Grant 61925108, and in part by the Joint fund of the National Natural Science Foundation of China and Robot Fundamental Research Center of Shenzhen Government under Grant U1913203, in part by the Natural Science Foundation China (NSFC) under Grant 61702336, 61902437, 62032015 and 61620106008, and in part by the Shenzhen Fundamental Research Program under Grant JCYJ2020010911041013. (*Corresponding author: Xiao Zhang.*)

Yu Zhou, Yu Chen and Jianmin Jiang are with the College of Computer Science and Software Engineering, Shenzhen University, Shenzhen 518060, China (email: yu.zhou@szu.edu.cn, 2070276225@email.szu.edu.cn, jianmin.jiang@szu.edu.cn).

Xiao Zhang and Pan lai are with the Department of Computer Science, South-Central Minzu University, Wuhan 430074, China (e-mail: xiao.zhang@my.cityu.edu.hk, plai1@ntu.edu.sg).

Lei Huang is with the College of Electronics and Information Engineering, Shenzhen University, Shenzhen 518060, China (e-mail: lhuang@szu.edu.cn).

mentioning that although parameter pruning techniques such as neural architecture search (NAS) can help to reduce the number of parameters [17], [18], the reconstruction quality is often limited due to the fact that, on the one hand, the manually designed complex network architecture fails to provide sufficient space for quality improvement, and on the other hand, unlike classification tasks, CS aims to reconstruct the data as accurately as possible; reducing the number of network parameters will ultimately degrade the reconstruction quality.

In recent years, recurrent learning has been introduced into vision tasks due to its excellent image-modeling capabilities. For example, DuDoRNet [19] shows that recurrent learning can better avoid overfitting by directly optimizing restoration networks in dual domains, and it can reconstruct high-quality images with a low number of parameters. PolSAR [20] is a novel recurrent learning strategy that learns polarization and spatial features from adjacent pixel sequences, which further reduces intraclass and interclass misclassifications. In addition, Adler et al. propose a sustainable CS approach that is mostly suitable for processing very high-dimensional images and videos: it operates on local patches, employs a low-complexity reconstruction operator and requires significantly less memory to store the sensing matrix [21]. Reddy et al. present an effective lightweight data-reduction method by investigating the performance of CS-based and partial discrete cosine transform (DCT)-based compression methods [22]. However, these methods still have some drawbacks; for example, they are not flexible enough, and the reconstruction quality depends on the complex design of the sampling matrix.

In smart cities, data come from different sources, and data collected and integrated through IoT devices are important. In this context, finding a balance between the accuracy of the data collection and the efficient use of limited resources through lightweight and efficient methods is critically important. In this paper, to realize a sustainable CS model, we focus on designing a lightweight but effective recurrent learning network called the compressed sensing recurrent network (CSRN). The proposed CSRN is based on a classical network structure that contains three sub-networks, namely, the sampling sub-network, initial reconstruction sub-network and residual reconstruction sub-network. While the sampling sub-network uses convolutional layers to perform the CS sampling process for original images, the initial reconstruction sub-network is used to recover an initial reconstructed image via linearly mapping measurements; the residual reconstruction sub-network is responsible for using nonlinear mapping to obtain high-frequency information and hence enhance the reconstructed details to provide higher-quality refinements. The final reconstructed image is obtained by integrating the initial reconstructed image and the residual image. Compared with existing approaches, our proposed CSRN differs in the following ways:

(1) We propose a flexible initial reconstruction sub-network consisting of basic recovery blocks to obtain initial images at different sample ratios, which can greatly reduce the number of network parameters.

(2) We propose a novel recurrent residual fusion module (RRFM) under the framework of recurrent learning to take

full advantage of features from different scales.

(3) We employ a feature compression strategy in the residual image reconstruction process to further improve the efficiency of the reconstruction process.

The remainder of this paper is organized as follows. First, CS and the related algorithms are described in Sec. II. Next, we describe the proposed method in Sec. III. In Sec. IV, we describe the extensive experiments that we performed and illustrate that our proposed algorithm outperforms a number of representative state-of-the-art methods. Finally, Sec. V provides concluding remarks.

II. RELATED WORK

A. Compressed Sensing

Compressed sensing is an emerging paradigm for signal processing that can be used to reconstruct sparse signals from a smaller number of linear measurements and thus greatly improve the efficiency and effectiveness of a sensing system. Mathematically, the sampling process of CS can be formulated as follows:

$$\mathbf{y} = \Phi \mathbf{x}, \quad (1)$$

where $\mathbf{x} \in R^N$ denotes the original signal, $\mathbf{y} \in R^M$ is the linear measurement and $\Phi \in R^{M \times N} (M \ll N)$ is the sampling matrix. In most cases, \mathbf{x} can be recovered by solving the following equation:

$$\min_{\mathbf{x}} \|\Psi \mathbf{x}\|_0, \text{ s.t. } \mathbf{y} = \Phi \mathbf{x}, \quad (2)$$

where Ψ is the sparse transform matrix, and $\|\cdot\|_0$ denotes the l_0 norm. However, solving l_0 optimization is an NP-hard problem; the solving process has a high complexity and may be unstable when noise interferes with the sampling process. The l_1 norm can be used to replace the l_0 norm to alleviate the above problems. Therefore, the signal can be recovered by solving

$$\min_{\mathbf{x}} \|\Psi \mathbf{x}\|_1, \text{ s.t. } \mathbf{y} = \Phi \mathbf{x}. \quad (3)$$

Eq. (3) is a convex problem, and its solution is equivalent to

$$\min_{\mathbf{x}} \|\mathbf{y} - \Phi \mathbf{x}\|_2^2 + \lambda \|\Psi \mathbf{x}\|_1, \quad (4)$$

where the first part and the second part are the fidelity term and regularization term, respectively, and λ is a parameter that is used to control the regularization strength.

B. Plain Deep Learning Network for Image Compressed Sensing

Inspired by the success of deep learning in computer vision tasks, many deep learning-based algorithms have been developed to overcome the shortcomings of traditional optimization-based algorithms.

Deep learning-based methods can be divided into two categories according to the network design. The first type of network is the plain network. This type of method attempts to directly learn a reconstruction algorithm from huge amounts of data. In [23], Mousavi et al. introduce deep learning into image CS and use a stacked denoising autoencoder to reconstruct images from measurements. Inspired by SRCNN, Kulkarni

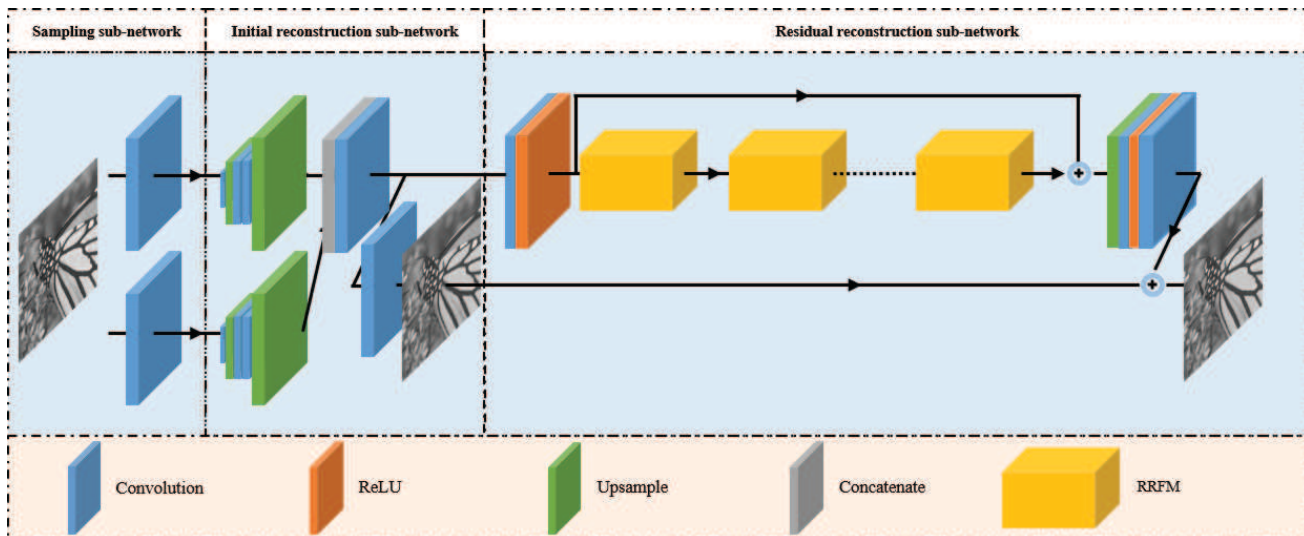


Fig. 1: Network architecture of the proposed CSRN when the sample ratio is 0.2. For the sampling process, two $Conv(102, 32, 32)$ layers are applied to mimic image sampling. For reconstruction, the initial reconstruction sub-network with a two-layer structure is used to reconstruct the initial image, and then the residual reconstruction sub-network is used to recover the residual image, which will be added to the initial image to obtain the final reconstructed image.

et al. propose ReconNet, which is based on a Convolutional neural network (CNN), in [24]; a fully connected layer and multiple convolutional layers are used to reconstruct images from measurements. In [25], Yao et al. propose Dr^2 -Net, which uses a linear mapping to reconstruct a preliminary image and then uses residual learning to further improve the image quality. However, Dr^2 -Net only learns the intra-block information and suffers from blocking artifacts. To solve this problem, in [26], DPA-Net is introduced; it has a dual path scheme to recover the image’s structure and texture, respectively, and an attention mechanism is also integrated into the network to boost the texture recovery. Moreover, Shi et al. propose CSNet, which uses residual networks to learn the map between the measurements and reconstructed image, to obtain fast end-to-end image reconstruction [27]. DPA-Net and CSNet both alleviate blocking artifacts to a certain extent. However, these types of completely data-driven models have poor interpretability due to their black-box characteristics.

C. Deep Unfolding Network for Image Compressed Sensing

The second category is the deep unfolding network; this type of network unfolds the iterative process of optimization-based methods using a neural network, which makes the network more interpretable. In [28], Zhang et al. propose ISTA-Net, which casts ISTA into a neural network form to combine the advantages of optimization-based methods and deep learning-based methods. AMP-Net [29] is proposed to unfold the iterative process of an approximate message mapping algorithm to reconstruct images. Further, AMP-Net uses a learnable deblocker to remove block artifacts to enhance the reconstruction quality. In [30], COAST is proposed to process an arbitrary sampling matrix using one deep unfolding model through random projection augmentation and a controllable proximal mapping module. Although these deep unfolding

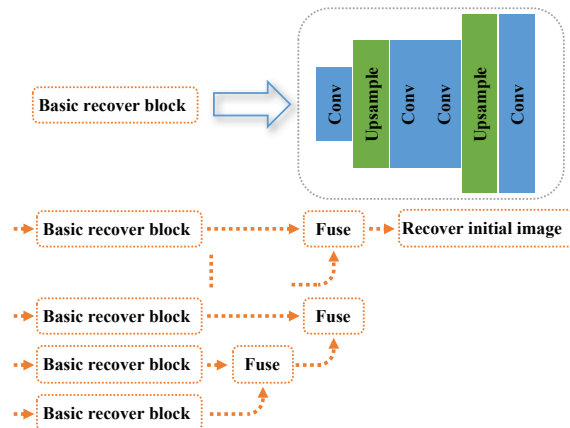


Fig. 2: The structure of the initial reconstruction sub-network when the sample ratio is greater than 0.1.

networks achieved good interpretability, it is still difficult to obtain a good reconstruction quality at a low sample ratio due to the network design.

Unlike the above-mentioned deep learning-based algorithms, our proposed method not only focuses on the quality of the reconstructed images but also pays attention to the computational resource consumption of the network. We carefully design our network to achieve the best possible balance between the image quality and resource consumption to create a sustainable CS imaging system.

III. PROPOSED METHOD

In this section, we discuss in detail the introduced RRFM, the proposed compression strategy and the overall architecture of the proposed CSRN. As shown in Fig. 1, the proposed network consists of three parts: a sampling sub-network, initial

reconstruction sub-network and residual reconstruction sub-network, which perform sampling, initial reconstruction and residual reconstruction, respectively. We use $Conv(n, k, s)$ to denote a convolutional layer and $PixelShuffle(u)$ to denote the pixel shuffle operation [31] for upsampling, where n is the number of kernels, k is the kernel size, s is the stride and u is the upsampling factor.

A. Sampling Sub-network

For CS tasks, the sampling step should be as simple as possible. Therefore, in the sampling sub-network, we follow [32] and use convolutional layers to sample original images. In traditional block compressed sensing, the image is first divided into small, non-overlapping $B \times B$ image blocks, and then these small blocks are sampled using the sampling matrix ϕ . This process can be mimicked by convolution, as the sampling operation is similar to convolution; each row of the sampling matrix can be replaced by a convolutional layer. For example, given the sample ratio r , the convolutional layer needs $\lfloor rB^2 \rfloor$ kernels with a kernel size of B and a stride of B to sample images. When the sample ratio is 0.1, we use $Conv(0.1 \times B^2, B, B)$ to sample the original image. Similarly, we use two $Conv(0.1 \times B^2, B, B)$ layers when the sample ratio is 0.2, and so on. Consequently, the sampling process can be expressed by

$$\mathbf{F}_m = f_s(\mathbf{x}), \quad (5)$$

where $f_s(\cdot)$ is the sampling operation, \mathbf{x} is the original image and \mathbf{F}_m represents the measurements. \mathbf{F}_m can be regarded as being composed of K groups of measurements. Each group of measurements \mathbf{F}_m^k contains $0.1 \times B^2$ feature maps.

Learning the sampling matrix using convolutional layers has two advantages. Compared with a manually designed matrix, on the one hand, the learned matrix takes the inherent characteristics of the signal into account, and on the other hand, the convolution operation guarantees that more structural information can be preserved during the sampling process. Therefore, sampling using convolutional layers guarantees a better reconstruction performance.

B. Initial Reconstruction Sub-network

According to previous studies, once measurements are obtained, a simple linear mapping can basically recover the original images [34]. We consider this discovery in designing our model and use an initial reconstruction sub-network to obtain initial reconstructed images. However, instead of using a single convolutional layer or fully connected layer to recover images, we use multiple convolutional layers to gradually increase the resolution of feature maps to recover images; we refer to the former method as simple initial reconstruction, while the latter method is referred to as progressive reconstruction.

Our initial reconstruction sub-network has a hierarchical structure. In other words, the structure of the initial reconstruction sub-network can be different if the corresponding sample ratio is different. When the sample ratio is below 0.1 (for example, if it is 0.05 or 0.01), the sub-network will use a basic recovery block to reconstruct images from process measurements. The basic recovery block contains $Conv(8m, 1, 1)$,

Algorithm 1 CSRN

Input: The original image \mathbf{x}

Output: The reconstructed image \mathbf{x}_f

```

1: /*Sampling the original image  $\mathbf{x}$  with the sampling sub-
   network*/
2:  $\mathbf{F}_m \leftarrow f_s(\mathbf{x})$ 
3: /*Recovering the initial reconstructed image  $\mathbf{x}_i$  with the
   initial reconstruction sub-network*/
4: for  $k = 1, 2, \dots, K$  do
5:    $\mathbf{F}_i^k \leftarrow f_r(\mathbf{F}_m^k)$ 
6:   if  $k \neq 1$  then
7:      $\mathbf{F}_i^k \leftarrow f_c([\mathbf{F}_i^{k-1}, \mathbf{F}_i^k])$ 
8:   end if
9: end for
10:  $\mathbf{x}_i \leftarrow f_i(\mathbf{F}_i^N)$ 
11: /*Recovering the residual image  $\mathbf{x}_r$  with the residual
   reconstruction sub-network*/
12:  $\mathbf{F}_c \leftarrow f_c(\mathbf{F}_i^N)$ 
13:  $\mathbf{F}_h \leftarrow f_e(\mathbf{F}_c)$ 
14:  $\mathbf{x}_r \leftarrow f_m(\mathbf{F}_c, \mathbf{F}_h)$ 
15: /*Adding the residual image and initial image to obtain
   the final reconstructed image  $\mathbf{x}_f$ */
16:  $\mathbf{x}_f = \mathbf{x}_i + \mathbf{x}_r$ 

```

$PixelShuffle(4)$, $Conv(m/2, 3, 1)$, $Conv(16m, 1, 1)$ and $PixelShuffle(8)$, where m denotes the number of convolution filters and the size of m is equal to B . The 1×1 convolution is designed to explore the information inside the block to recover images, and after the first 1×1 convolution and upsampling operation, the resolution of the feature maps is increased to one eighth of the resolution of the original image. Then, 3×3 convolution is used to extract the information between blocks to mitigate the problem of block artifacts. Then, the second 1×1 convolution and upsampling operation increases the resolution of the feature maps to the resolution of the original image. Finally, $Conv(1, 3, 1)$ is used to generate the initial reconstructed image. This process can be described as follows:

$$\mathbf{F}_i = f_r(\mathbf{F}_m), \quad (6)$$

$$\mathbf{x}_i = f_i(\mathbf{F}_i), \quad (7)$$

where $f_r(\cdot)$ is used to obtain feature maps with the same resolution as the original images, \mathbf{F}_i represents intermediate feature maps with the resolution of the original images and $f_i(\cdot)$ is the operation for reconstructing the initial image \mathbf{x}_i .

When the sample ratio is greater than 0.1, the sub-network will stack basic recovery blocks to process measurement groups and generate intermediate feature maps \mathbf{F}_i^k . A series of concatenation and convolution operations are then applied to fuse these intermediate feature maps. Finally, $Conv(1, 3, 1)$ is used to generate an initial image. For example, when the sample ratio is 0.2, $Conv(m/2, 1, 1)$ is used to fuse \mathbf{F}_i^1 and \mathbf{F}_i^2 , and $Conv(1, 3, 1)$ is used to generate the initial image. The details of this operation are given below:

$$\mathbf{F}_i^2 = f_c([\mathbf{F}_i^1, \mathbf{F}_i^2]), \quad (8)$$

$$\mathbf{x}_i = f_i(\mathbf{F}_i^2), \quad (9)$$

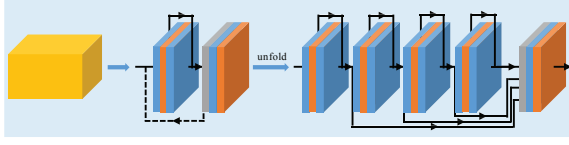


Fig. 3: Recurrent residual fusion module. The dotted line denotes the recurrent connection.

where $[\cdot]$ denotes the concatenation operation and f_c is the fuse operation performed using $1*1$ convolution. A sketch describing the structure of the initial reconstruction sub-network when the sample ratio is greater than 0.1 is shown in Fig. 2.

C. Residual Reconstruction Sub-network

Following the generation of the initially reconstructed image, a residual reconstruction sub-network is applied to generate the residual image in order to preserve the high-frequency details. The residual reconstruction sub-network includes a feature compression module (FCM), a feature extraction module (FEM) with N RRFMs and a feature fusion module (FFM).

As described before, the FCM is located at the head of the residual reconstruction network, and the feature map \mathbf{F}_i^k is used as the input of the FCM; the feature map \mathbf{F}_i^k is compressed to obtain the feature map \mathbf{F}_c , which has a reduced size:

$$\mathbf{F}_c = f_{FCM}(\mathbf{F}_i^k), \quad (10)$$

where $f_{FCM}(\cdot)$ denotes the feature compression operation, and \mathbf{F}_c represents the compressed feature maps. The FCM is described in detail in subsection E.

The FEM is in the middle of the sub-network, and it stacks N RRFMs to extract features from \mathbf{F}_c :

$$\mathbf{F}_h = f_{FEM}(\mathbf{F}_c). \quad (11)$$

\mathbf{F}_h is the output of the FEM. The specific implementation of the RRFM will be presented in subsection D.

The FFM is located at the end of the sub-network. It can upsample feature maps to recover the original resolution and it fuses feature maps to obtain the residual image. First, the FFM adds \mathbf{F}_c to \mathbf{F}_h ; then, it uses $Conv(m, 3, 1)$ and the ReLU activation function to further process the feature maps. Following that, $PixelShuffle(2)$ is used to upsample the feature maps. In the end, $Conv(1, 3, 1)$ is used to generate the residual image:

$$\mathbf{x}_r = f_{FFM}(\mathbf{F}_c + \mathbf{F}_h), \quad (12)$$

where \mathbf{x}_r is the residual image and f_{FFM} is the FFM operation. The final reconstructed image can be generated by adding the residual image and the initial reconstructed image:

$$\mathbf{x}_f = \mathbf{x}_i + \mathbf{x}_r. \quad (13)$$

The pseudocode of CSRN is shown in Algorithm 1.

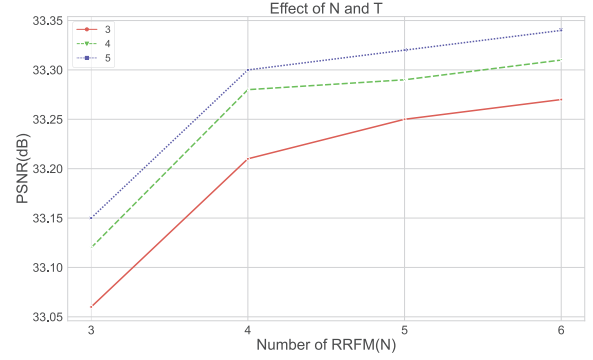


Fig. 4: Reconstruction performance on Set5 for different combinations of N and T .

D. Recurrent Residual Fusion Module

The proposed recurrent residual fusion module (RRFM) is composed of a residual block and a convolutional layer. When feature maps flow through the RRFM, the residual block will first recurrently process these features, which means that the output of the residual block from the previous recurrence will be the input of the next recurrence. As the recurrence goes on, the receptive field gradually increases, and thus information about the object from different scales can be extracted. Then, the multi-scale intermediate features obtained by each recurrence will be concatenated. Finally, the convolutional layer will fuse these concatenated feature maps; the fused feature maps are the output of the RRFM.

The residual block was proposed in [33] to facilitate gradient propagation; it consists of a convolutional layer, batch normalization (BN) layer and activation function. It has shown great success in many computer tasks. However, the original design of the residual block is high-level-vision-task-oriented and thus not suitable for low-level vision tasks due to the fact that the BN layer causes the network to lose flexibility through feature normalization. Therefore, EDSR [34] removes the BN layer in the residual block and thus achieves a better performance in the super-resolution area. Since image compressive sensing is essentially a low-level vision task, we adopt this improved residual block in our network. The convolutional layer in the RRFM accepts intermediate feature maps generated by the residual block during recurrence and performs feature fusion. Therefore, we set both the kernel size and the stride of the convolutional layer to 1, that is, $Conv(m, 1, 1)$ is used.

As shown in Fig. 3, due to the recurrent structure of the RRFM, it can be unfolded into T residual blocks with shared parameters and a convolutional layer. The output \mathbf{F}_r of the RRFM is

$$\mathbf{F}_r = f_{fuse}([\mathbf{R}^1, \mathbf{R}^2, \dots, \mathbf{R}^t]), \quad (14)$$

where $t = 1, 2, \dots, T$, \mathbf{R}^t represents the intermediate features generated by the n th recurrence, $[\cdot]$ denotes the concatenation operation and $f_{fuse}(\cdot)$ denotes the feature fusion operation performed using $Conv(m, 1, 1)$.

E. Feature Compression Strategy

To speed up and reduce the memory consumption of the image reconstruction process, we introduce a feature compression strategy into the residual reconstruction sub-network. This strategy compresses the size of feature maps. We justify the introduction of such a compression strategy using the following argument. Since the initial reconstruction sub-network can reconstruct a relatively good initial image, the residual module does not need to retain the feature maps with the original resolution of the image to obtain its high-frequency details. Therefore, the feature compression module (FCM) is placed at the head of the residual reconstruction sub-network to perform the compression operation. This block takes feature maps from the initial reconstruction sub-network as the input and compresses the feature maps to a quarter of their original size; then, it passes the compressed feature maps to the rest of the residual reconstruction network for further processing.

We use $Conv(m, 2, 2)$ and the ReLU activation function to form the FCM. The stride convolution layer can compress feature maps to one quarter of their original size, and thus the benefits of compressing feature maps are obvious. First, the compressed feature maps take up less memory, so a deeper network can be constructed for a better performance without having to consider the memory consumption. Second, the number of calculations will be reduced, along with the burden placed on the computing devices being used.

IV. EXPERIMENTAL STUDIES

In this section, we will introduce the settings and datasets used in the experiments. Our proposed network will be compared with representative existing methods, and the contributions of each individual part of our proposed network will also be analyzed and discussed.

A. Settings and Datasets

To evaluate our proposed network, we use 7 sample ratios, including 0.01, 0.05, 0.1, 0.2, 0.3, 0.4 and 0.5; we use 400 images from BSDS500 [35] as the training set and 100 images as the validation set. Each image of the training set is cropped into small 96×96 pieces. Eight data augmentation methods described in [36] are further applied to make full use of these images. As a result, we have in total 89600 image pieces for training and 22400 image pieces for validation. The Adam optimizer is used to train CSRN with a batch size of 16 for 100 epochs. The learning rate starts at 0.0005 and decreases by a factor of 0.1 at the 50th and 80th epochs. Higher learning rates at the beginning of training are more likely to suppress the memory of noisy data and speed up training, while lower learning rates in the middle and later stages of training make it easier to find the global optimal solution. The number of convolution filters m is set to 32. We use the mean square

error(MSE) loss of the initial reconstructed image and final reconstructed image to guide the gradient descent process:

$$\Theta(\Lambda) = \arg \min_{\theta_s, \theta_i, \theta_r} \frac{1}{2M} \sum_{i=1}^M \|g(\mathbf{x}^i; \theta_s, \theta_i) - \mathbf{x}^i\|_2^2 + \frac{1}{2M} \sum_{i=1}^M \|g(\mathbf{x}^i; \theta_s, \theta_i, \theta_r) - \mathbf{x}^i\|_2^2, \quad (15)$$

where Λ denotes the collection of model parameters, θ_s , θ_i and θ_r denote the parameters of the sampling sub-network, initial reconstruction sub-network and residual reconstruction sub-network, respectively, $g(\cdot)$ represents the network's operation, $g(\mathbf{x}^i; \theta_s, \theta_i)$ denotes the initial reconstructed image and $g(\mathbf{x}^i; \theta_s, \theta_i, \theta_r)$ denotes the final reconstructed image. We take the model that obtains the smallest loss on the validation set as our final model and test its performance. We implement the proposed network in PyTorch, and we train and test our models on an NVIDIA Titan Xp.

The Set5 [37], Set11 [24], Set14 [38], BSD100 [39], Urban100 [40] and DIV2K validation sets [41] are used as test datasets in our experiments. We measure the reconstruction quality using the peak signal-to-noise ratio (PSNR) [42] and structural similarity index (SSIM) [43]. Like other CS algorithms [44], [45], we convert the image from the RGB space into the YCbCr space and take the luminance channel as the input.

B. Determining the Values of N and T

To choose the best combination of N and T , we combine different numbers of RRFMs (N) with different numbers of recurrences (T) in the residual reconstruction sub-network for a sample ratio of 0.1 and test the performance of this sub-network on Set5.

The results are shown in Fig. 4; we can see that using more RRFMs and increasing the number of recurrences leads to a better reconstruction quality. Stacking more RRFMs and making the network deeper make it possible to extract more meaningful features for high-frequency details and hence enrich the reconstructions. Furthermore, when N is large, increasing T can still improve the reconstruction quality, but the improvement is not as obvious as when N is small. Although increasing N and T could provide better performances, the network will use more memory and time for reconstruction. Hence, after weighing the performance of the network against the resources required by the network, we set N to 5 and T to 3 in our experiments.

C. Comparison with State-of-the-Art Methods

To provide a comprehensive evaluation of our proposed method, we compare the proposed method with DWT [6], MH [46], GSR [7], ReconNet [24], Dr²-Net [25], DPA-Net [26], SCSNet [47], CSNet⁺ [32], ISTA-Net⁺ [28], ISTA-Net⁺⁺ [48], OPINE-Net [35] and COAST [30]; the first three methods are optimization-based methods, the middle five methods are plain networks and the last four methods are deep unfolding networks. For all of these methods, we used the recommended

TABLE I: Reconstruction Quality Comparison of CSRN, Optimization-Based Algorithms and Plain Networks

Algorithm	0.01		0.05		0.1		0.2		0.3		0.4		0.5		Average	
	PSNR(dB)	SSIM														
Set5																
DWT	13.76/0.4419		23.11/0.6831		26.58/0.7601		29.74/0.8366		31.98/0.8790		33.81/0.9077		35.53/0.9299		27.79/0.7769	
MH	15.38/0.3718		25.25/0.7192		28.57/0.8211		31.97/0.8859		33.73/0.9123		35.27/0.9324		36.86/0.9474		29.57/0.7986	
GSR	21.03/0.5882		26.97/0.7944		30.48/0.8754		34.54/0.9286		36.94/0.9498		38.85/0.9627		40.65/0.9724		32.78/0.8674	
ReconNet	20.34/0.5347		25.26/0.7039		28.03/0.7943		30.77/0.8597		32.36/0.8905		34.21/0.9172		34.92/0.9273		29.41/0.8039	
Dr ² -Net	20.37/0.5384		25.56/0.7205		28.50/0.8180		31.49/0.8813		33.71/0.9178		35.40/0.9366		37.08/0.9522		30.30/0.8235	
DPA-Net	19.02/0.5133		26.66/0.7893		29.29/0.8705		32.54/0.9019		34.57/0.9412		36.13/0.9575		37.51/0.9679		30.82/0.8488	
SCSNet	24.21/0.6468		29.74/0.8472		32.77/0.9083		36.15/0.9487		38.45/0.9655		40.44/0.9755		42.22/0.9820		34.85/0.8963	
CSNet ⁺	24.23/0.6492		29.80/0.8506		32.65/0.9078		36.21/0.9489		38.53/0.9656		40.32/0.9750		42.27/0.9819		34.85/0.8970	
CSRN	24.53/0.6628		30.39/0.8638		33.25/0.9155		36.61/0.9518		38.83/0.9673		40.72/0.9765		42.59/0.9830		35.27/0.9030	
Set11																
DWT	13.24/0.3731		21.23/0.5980		23.41/0.6852		26.32/0.7840		28.43/0.8407		30.34/0.8806		32.14/0.9105		25.02/0.7246	
MH	14.11/0.3374		22.24/0.6545		26.07/0.7873		29.39/0.8671		31.51/0.9039		33.29/0.9266		34.90/0.9438		27.36/0.7744	
GSR	18.19/0.4874		24.05/0.7516		28.12/0.8585		32.25/0.9216		34.77/0.9461		36.87/0.9614		38.71/0.9716		30.42/0.8426	
ReconNet	17.83/0.4541		22.07/0.6276		24.65/0.7345		27.30/0.8170		28.89/0.8546		30.90/0.8941		31.60/0.9064		26.18/0.7555	
Dr ² -Net	17.87/0.4595		22.40/0.6449		25.16/0.7568		28.12/0.8399		30.33/0.8845		32.06/0.9114		33.77/0.9329		27.10/0.7757	
DPA-Net	18.20/0.5101		23.77/0.7811		27.66/0.8530		30.47/0.9087		33.35/0.9425		35.21/0.9580		36.80/0.9685		29.35/0.8460	
SCSNet	21.04/0.5601		25.79/0.7878		28.48/0.8630		31.97/0.9229		34.62/0.9512		36.92/0.9652		39.01/0.9767		31.12/0.8610	
CSNet ⁺	21.02/0.5586		25.98/0.7891		28.54/0.8632		32.02/0.9230		34.70/0.9511		36.80/0.9657		39.03/0.9768		31.16/0.8611	
CSRN	21.40/0.5751		26.57/0.8076		29.00/0.8733		32.55/0.9293		35.21/0.9556		37.49/0.9699		39.60/0.9790		31.69/0.8700	
Set14																
DWT	14.83/0.4097		22.44/0.5939		24.73/0.6684		27.43/0.7584		29.32/0.8159		31.00/0.8589		32.63/0.8925		26.05/0.7140	
MH	15.16/0.3517		23.47/0.6156		26.38/0.7433		29.48/0.8228		31.29/0.8674		32.89/0.8989		34.43/0.9225		27.59/0.7460	
GSR	20.32/0.5124		24.67/0.6756		27.87/0.7775		31.40/0.8622		33.80/0.9046		35.82/0.9322		37.64/0.9513		30.22/0.8022	
ReconNet	19.44/0.4639		23.52/0.6033		25.64/0.6916		27.78/0.7689		29.13/0.8135		30.86/0.8594		31.45/0.8751		26.83/0.7251	
Dr ² -Net	19.48/0.4683		23.79/0.6154		25.94/0.7066		28.33/0.7912		30.40/0.8481		31.87/0.8835		33.35/0.9096		27.59/0.7461	
DPA-Net	18.30/0.4616		24.71/0.7286		26.28/0.7693		31.47/0.8845		30.86/0.8978		32.30/0.9246		33.78/0.9440		28.24/0.8015	
SCSNet	22.87/0.5631		26.92/0.7322		29.22/0.8181		32.19/0.8945		34.51/0.9311		36.54/0.9525		38.41/0.9659		31.52/0.8368	
CSNet ⁺	22.77/0.5577		26.88/0.7313		29.11/0.8167		32.19/0.8942		34.52/0.9306		36.41/0.9514		38.39/0.9656		31.47/0.8354	
CSRN	23.04/0.5722		27.23/0.7428		29.43/0.8251		32.48/0.8993		34.75/0.9340		36.73/0.9546		38.72/0.9674		31.77/0.8422	
BSD100																
DWT	15.39/0.4135		23.12/0.5765		24.98/0.6449		27.14/0.7332		28.75/0.7938		30.25/0.8407		31.70/0.8781		25.90/0.6972	
MH	16.41/0.3730		23.67/0.5865		25.16/0.6673		28.11/0.7733		29.74/0.8287		31.22/0.8688		32.65/0.8998		26.71/0.7139	
GSR	21.14/0.4997		23.95/0.6204		25.98/0.7094		28.79/0.8075		30.98/0.8662		32.93/0.9059		34.77/0.9340		28.36/0.7633	
ReconNet	20.87/0.4761		24.08/0.5905		25.74/0.6698		27.49/0.7434		28.66/0.7904		30.29/0.8450		30.91/0.8641		26.86/0.7113	
Dr ² -Net	20.92/0.4808		24.25/0.5984		25.98/0.6815		28.07/0.7689		29.80/0.8308		31.26/0.8731		32.75/0.9045		27.57/0.7340	
DPA-Net	19.00/0.4487		23.51/0.6771		25.37/0.7219		27.78/0.8413		29.55/0.8735		31.05/0.9089		32.44/0.9341		26.96/0.7722	
SCSNet	23.78/0.5483		26.77/0.6972		28.57/0.7844		31.10/0.8731		33.24/0.9190		35.21/0.9470		37.14/0.9649		30.83/0.8191	
CSNet ⁺	23.76/0.5478		26.81/0.6990		28.60/0.7847		31.13/0.8730		33.29/0.9194		35.21/0.9467		37.17/0.9649		30.85/0.8194	
CSRN	23.98/0.5564		27.01/0.7067		28.79/0.7916		31.35/0.8777		33.45/0.9220		35.39/0.9487		37.33/0.9661		31.04/0.8242	
Urban100																
ReconNet	17.94/0.4303		21.26/0.5705		23.23/0.6670		25.28/0.7523		26.50/0.7958		28.30/0.8481		28.79/0.8624		24.47/0.7038	
Dr ² -Net	17.97/0.4351		21.54/0.5876		23.73/0.6951		26.17/0.7884		28.21/0.8471		29.70/0.8810		31.29/0.9097		25.52/0.7349	
DPA-Net	16.36/0.4162		22.88/0.6404		24.55/0.7851		28.82/0.8093		29.48/0.9044		31.10/0.9319		32.09/0.9454		26.47/0.7761	
SCSNet	20.65/0.5196		24.37/0.7171		26.61/0.8093		29.60/0.8915		32.01/0.9310		34.07/0.9531		36.10/0.9680		29.06/0.8271	
CSNet ⁺	20.69/0.5199		24.38/0.7171		26.63/0.8098		29.65/0.8917		32.04/0.9311		34.12/0.9533		36.12/0.9681		29.09/0.8273	
CSRN	20.89/0.5314		24.74/0.7336		26.96/0.8225		30.09/0.9005		32.43/0.9359		34.52/0.9570		36.43/0.9704		29.44/0.8359	
DIV2K validation set																
ReconNet	21.81/0.5862		25.81/0.7001		27.89/0.7704		29.99/0.8301		31.38/0.8644		33.16/0.9004		33.79/0.9124		29.12/0.7949	
Dr ² -Net	21.87/0.5922		26.07/0.7113		28.24/0.7842		30.73/0.8508		32.72/0.8938		34.32/0.9209		35.92/0.9407		29.98/0.8134	
DPA-Net	19.79/0.5508		26.81/0.7648		28.21/0.8219		31.69/0.8711		33.02/0.9197		34.49/0.9420		35.97/0.9577		30.00/0.8326	
SCSNet	25.17/0.6631		29.10/0.8010		31.35/0.8673		34.34/0.9251		36.71/0.9525		38.88/0.9688		40.41/0.9699		33.71/0.8782	
CSNet ⁺	25.15/0.6630		29.11/0.8010		31.34/0.8671		34.36/0.9254		36.73/0.9528		38.86/0.9686		40.86/0.9786		33.77/0.8795	
CSRN	25.41/0.6708		29.42/0.8090		31.65/0.8731		34.69/0.9293		37.05/0.9553		39.15/0.9703		41.16/0.9798		34.08/0.8839	

parameter settings and the code implementations provided by the authors. Particularly, since OPINE-Net and COAST apply multiple sampling matrices within one network, for a fair comparison and to focus on the reconstruction ability of our CSRN, we only use a single learned sampling matrix for both of these methods. We calculate the reconstruction quality of deep learning-based methods on all six test datasets, but we test the optimization-based methods only on Set5, Set11, Set14 and BSD100 since optimization-based methods take too much time on the Urban100 and DIV2K validation sets.

Comparison with optimization-based algorithms and plain deep networks: We first compare CSRN with optimization-based algorithms and plain deep networks. The results are shown in Table I, where it can be seen that compared with optimization-based methods, deep learning-based methods have a better reconstruction quality in most cases. As DWT and MH use a manual sparse basis to process CS measurements, they have relatively poor performances. GSR merges group sparsity into the reconstruction process and thus is capable of further exploring the image information.

TABLE II: Reconstruction Quality Comparison of CSRN and Deep Unfolding Networks

Algorithm	0.1		0.2		0.3		0.4		0.5		Average	
	PSNR(dB)	SSIM										
Set5												
ISTA-Net ⁺	30.31/0.8627		34.37/0.9218		36.90/0.9471		38.91/0.9611		40.71/0.9733		36.24/0.9332	
ISTA-Net ⁺⁺	30.22/0.8702		33.94/0.9250		36.27/0.9485		38.13/0.9621		39.95/0.9725		35.70/0.9357	
COAST	30.50/0.8794		34.18/0.9298		36.48/0.9515		38.33/0.9645		40.21/0.9744		35.94/0.9399	
OPINE-Net	32.51/0.9150		35.55/0.9471		37.44/0.9579		39.84/0.9648		41.62/0.9805		37.39/0.9531	
CSRN	33.25/0.9155		36.61/0.9518		38.83/0.9673		40.72/0.9765		42.59/0.9830		38.40/0.9588	
Set11												
ISTA-Net ⁺	27.02/0.8135		31.12/0.9002		34.00/0.9359		36.17/0.9549		38.07/0.9706		33.28/0.9150	
ISTA-Net ⁺⁺	28.34/0.8531		32.33/0.9217		34.86/0.9478		36.94/0.9628		38.73/0.9727		34.24/0.9316	
COAST	28.69/0.8618		32.54/0.9251		35.04/0.9501		37.13/0.9648		38.94/0.9744		34.47/0.9352	
OPINE-Net	29.81/0.8904		32.51/0.9291		34.57/0.9328		36.17/0.9533		40.19/0.9800		34.65/0.9371	
CSRN	29.00/0.8733		32.55/0.9293		35.21/0.9556		37.49/0.9699		39.60/0.9790		34.77/0.9414	
Set14												
ISTA-Net ⁺	27.31/0.7478		30.86/0.8476		33.45/0.8959		35.51/0.9276		37.08/0.9525		32.84/0.8743	
ISTA-Net ⁺⁺	27.32/0.7714		30.72/0.8628		33.07/0.9074		34.98/0.9341		36.73/0.9525		32.56/0.8856	
COAST	27.41/0.7799		30.71/0.8672		33.10/0.9106		35.12/0.9369		36.94/0.9549		32.66/0.8899	
OPINE-Net	28.77/0.8294		31.82/0.8847		33.59/0.9315		36.19/0.9424		38.09/0.9662		33.69/0.9108	
CSRN	29.43/0.8251		32.48/0.8993		34.75/0.9340		36.73/0.9546		38.72/0.9674		34.42/0.9161	
BSD100												
ISTA-Net ⁺	26.79/0.7138		29.54/0.8161		31.67/0.8751		33.53/0.9130		35.05/0.9404		31.32/0.8517	
ISTA-Net ⁺⁺	26.15/0.7261		28.85/0.8301		30.91/0.8866		32.80/0.9225		34.63/0.9470		30.67/0.8625	
COAST	26.18/0.7297		28.83/0.8302		30.86/0.8851		32.71/0.9204		34.49/0.9450		30.61/0.8621	
OPINE-Net	27.55/0.7903		29.58/0.8526		32.17/0.8942		33.98/0.9382		36.02/0.9627		31.86/0.8876	
CSRN	28.79/0.7916		31.35/0.8777		33.45/0.9220		35.39/0.9487		37.33/0.9661		33.26/0.9012	
Urban100												
ISTA-Net ⁺	25.38/0.7572		29.42/0.8703		32.29/0.9195		34.59/0.9466		36.74/0.9641		31.68/0.8915	
ISTA-Net ⁺⁺	25.53/0.7882		29.36/0.8867		31.93/0.9280		33.99/0.9504		35.84/0.9646		31.33/0.9036	
COAST	25.94/0.8038		29.70/0.8940		32.20/0.9317		34.21/0.9528		35.99/0.9665		31.61/0.9098	
OPINE-Net	26.61/0.8362		30.01/0.8942		32.38/0.9318		34.19/0.9505		36.62/0.9727		31.96/0.9171	
CSRN	26.96/0.8225		30.09/0.9005		32.43/0.9359		34.52/0.9570		36.43/0.9704		32.09/0.9173	
DIV2K validation set												
ISTA-Net ⁺	29.40/0.8139		32.71/0.8894		35.15/0.9276		37.19/0.9504		39.22/0.9661		34.73/0.9095	
ISTA-Net ⁺⁺	28.96/0.8209		32.11/0.8944		34.41/0.9304		36.38/0.9517		38.22/0.9656		34.02/0.9126	
COAST	29.16/0.8279		32.22/0.8972		34.45/0.9318		36.40/0.9528		38.22/0.9668		34.09/0.9153	
OPINE-Net	30.64/0.8713		32.98/0.9184		35.63/0.9422		38.07/0.9678		39.88/0.9767		35.44/0.9353	
CSRN	31.65/0.8731		34.69/0.9293		37.05/0.9553		39.15/0.9703		41.16/0.9798		36.74/0.9416	

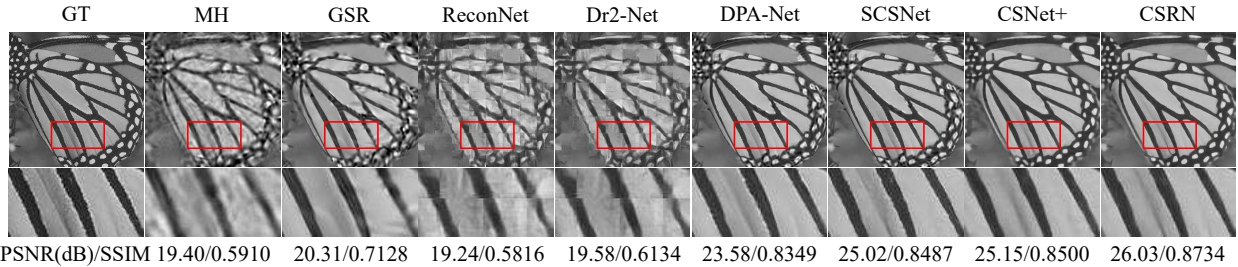


Fig. 5: Visual quality comparison of different optimization- and plain-network-based CS algorithms on “Butterfly” from Set5 for the sample ratio 0.05.

ReconNet has a simple network structure, yet its performance is better than that of DWT but worse than that of GSR. Dr²-Net introduces a residual connection into its network structure, and its reconstruction performance is better than that of ReconNet. Furthermore, it is worthwhile to note that ReconNet and Dr²-Net can achieve better results than DWT and MH when sample ratios less than 0.05 are used, which shows the potential of deep learning-based CS algorithms at low sample ratios. DPA-Net, SCSNet and CSNet⁺ have more sophisticated structures, so their reconstruction qualities surpass those of optimization-based methods. CSRN achieves the best average reconstruction quality out of all eight compared methods on

all test sets. Compared with the second-best method, CSRN improves the PSNR by 0.42, 0.53, 0.25, 0.19, 0.35 and 0.31 dB on average, and it improves the SSIM by 0.0060, 0.0089, 0.0054, 0.0048, 0.0086 and 0.0044 on average on Set5, Set11, Set14, BSD100, Urban100 and DIV2k, respectively. All the experimental results validate the effectiveness of our proposed CSRN.

Some reconstructed samples are illustrated in Fig. 5 and Fig. 6 for visual inspection, and we can observe that the images reconstructed by optimization-based methods have some noise, which impairs the visual quality of the reconstructed images. As shown, the images reconstructed by MH have severe

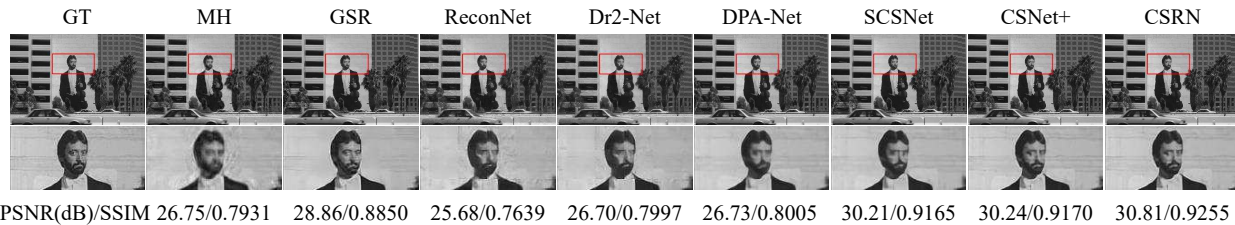


Fig. 6: Visual quality comparison of different optimization- and plain-network-based CS algorithms on “119082” from BSD100 for the sample ratio 0.2.

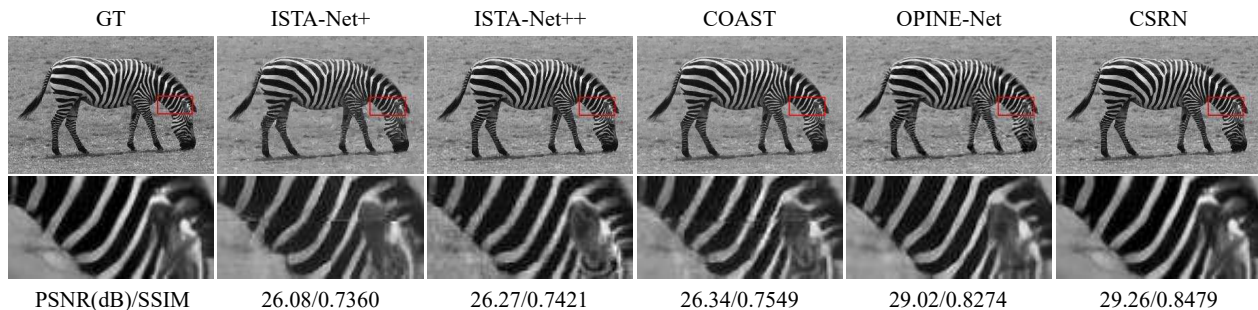


Fig. 7: Visual quality comparison of different deep unfolding network-based CS algorithms on “Zebra” from Set14 for the sample ratio 0.1.

blurring and artifacts that affect the visual appearance. GSR performs best out of the optimization methods; it works well for smooth areas of the image but still produces serious artifacts in areas with more texture. For plain deep networks, ReconNet and Dr²-Net produce significant blocky artifacts, while DPA-Net, SCSNet and CSNet⁺ present a better visual quality by using a deeper feature extraction structure to retain smooth structures. However, the boundary or intersection between the different structures is usually blurred or over-smoothed, which indicates that some details have been lost. Compared with these methods, our proposed CSRN not only maintains a structural smoothness but also reconstructs more boundary details through multi-scale feature fusion and the recurrent learning process.

Comparison with deep unfolding networks: We further compare CSRN with deep unfolding networks and show the results in Table II. It can be seen that due to their physics-driven structures, ISTA-Net and OPINE-Net obtain a better reconstruction quality under some circumstances, but CSRN still achieves a better average reconstruction quality compared with deep unfolding algorithms. All of the above experimental results validate the effectiveness of our proposed CSRN.

The visual results are displayed in Fig. 7, Fig. 8 and Fig. 9. ISTA-Net⁺, ISTA-Net⁺⁺ and COAST perform well in recovering the in-block information of images, but they incur some block artifacts due to the fact that they reconstruct each image block independently. To solve the block artifacts problem, OPINE-Net extends the intra-block training to inter-block training to enhance the CS recovery quality. CSRN can better mitigate these artifacts because the model optimizes the whole image, not just small image patches, during the training stage. Compared with these methods, CSRN recovers images

more clearly due to its effective network design. In particular, CSRN retains more details and has better visual effects. Therefore, it is concluded that CSRN has a better performance according to both subjective and objective evaluations.

Reconstruction time comparison: The average reconstruction times for 256×256 images achieved by CSRN and the compared algorithms are summarized in Table III. Overall, compared with optimization-based methods, deep learning methods reconstruct images much faster due to their non-iterative nature. The three considered optimization-based methods take roughly a few seconds to several minutes to reconstruct an image. CSRN is significantly faster than most of the deep learning-based algorithms, including DPA-Net, SCSNet, ISTA-Net⁺, ISTA-Net⁺⁺, COAST and OPINE-Net. CSRN employs a recurrent structure, which deepens the network, and thus its time is comparable to that of CSNet⁺. Although ReconNet and Dr²-Net run faster than CSRN, both of them employ a shallow structure that fails to reconstruct the details perfectly, thus resulting in low PSNR and SSIM values compared with CSRN. In short, CSRN can reconstruct images faster than its competitors and maintain a high reconstruction quality.

Parameter comparison: Furthermore, we count each model’s parameters and list the results in Table IV. For models that include sampling and reconstruction components, like SCSNet, CSNet⁺, ISTA-Net⁺, ISTA-Net⁺⁺, COAST, OPINE-Net and CSRN, we count the reconstruction component’s parameters. As shown, DPA-Net has the most parameters under all sample ratios, followed by COAST, while ReconNet has the fewest parameters when the sample ratio is less than 0.1; CSRN has the fewest parameters when the sample ratio is higher than 0.1. In fact, precisely because the progressive

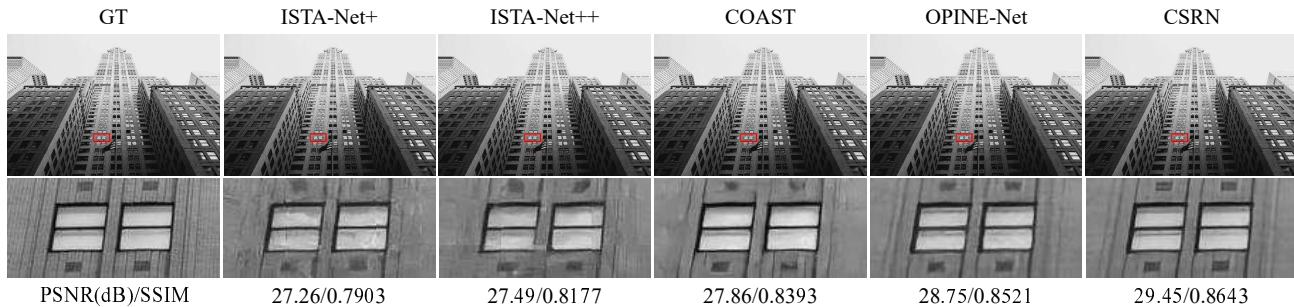


Fig. 8: Visual quality comparison of different deep-unfolding-network-based CS algorithms on “0846” from DIV2K for a sample ratio of 0.1.

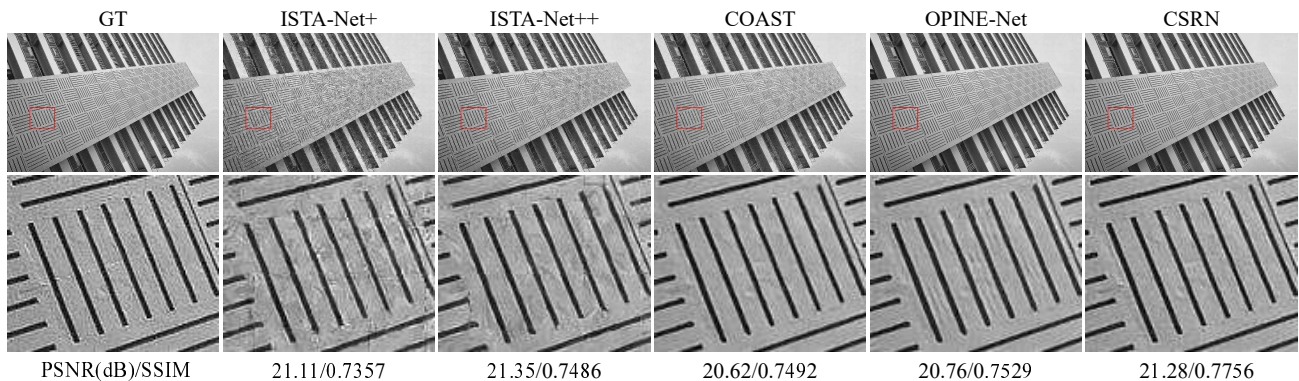


Fig. 9: Visual quality comparison of different deep-unfolding-network-based CS algorithms on “img 092” from Urban100 for a sample ratio of 0.2.

initial reconstruction sub-network constantly reconstructs the image by fusing feature maps, at high sample ratios, our initial reconstruction module can significantly reduce the number of parameters. Compared with other methods, CSRN uses progressive initial reconstruction and a recurrent structure, so it does not need as many parameters. While CSRN has more parameters than ReconNet and Dr²-Net for sample ratios less than 0.1, it has a better reconstruction quality; Fig. 10 provides an intuitive illustration of this. As a result, our proposed CSRN achieves a good balance between the number of parameters and the quality of the reconstructions. In other words, CSRN not only achieves a better reconstruction quality but also has a competitive reconstruction speed and a relatively small number of parameters.

D. Analysis of Progressive Initial Reconstruction

In our experiments, the simple initial reconstruction process uses a simple convolutional layer to perform dimensional mapping. Our initial reconstruction sub-network has a hierarchical structure and progressively recovers the original images, meaning that it needs fewer parameters for initial reconstructions. Table V compares the parameters needed for simple initial reconstruction and progressive initial reconstruction. When the sample ratio is 0.01, progressive initial reconstruction requires slightly more parameters than simple initial reconstruction. At high sample ratios, however, progressive initial reconstruction requires significantly fewer parameters. As an example, pro-

TABLE III: Time Consumption Comparison of Different Methods

Algorithm	Time (s)	Device
DWT	6.2973	Intel Core i7-7770
MH	6.6910	Intel Core i7-7770
GSR	821.2338	Intel Core i7-7770
ReconNet	0.0013	NVIDIA Titan Xp
Dr ² -Net	0.0016	NVIDIA Titan Xp
DPA-Net	0.0311	NVIDIA Titan Xp
SCSNet	0.0283	NVIDIA Titan Xp
CSNet ⁺	0.0025	NVIDIA Titan Xp
ISTA-Net ⁺	0.0071	NVIDIA Titan Xp
ISTA-Net ⁺⁺	0.0123	NVIDIA Titan Xp
COAST	0.0163	NVIDIA Titan Xp
OPINE-Net	0.0209	NVIDIA Titan Xp
CSRN	0.0022	NVIDIA Titan Xp

gressive initial reconstruction requires one third of the number of parameters required by simple initial reconstruction when the sample ratio is 0.5.

To investigate the effect of progressive initial reconstruction on the quality of the initial reconstructed image, we replace it with simple initial reconstruction and test the quality of the initial reconstructed images from DIV2K; the results of this comparison are listed in Table VI. It can be observed that progressive initial reconstruction can achieve a better quality at low sample ratios, but its reconstruction quality is not more advantageous at high sample ratios. This is partly due to the

TABLE IV: Comparison of the Number of Parameters (K) of Deep Learning CS Networks

Algorithm	Sample Ratio						
	0.01	0.05	0.1	0.2	0.3	0.4	0.5
ReconNet	34	76	128	234	338	444	548
Dr ² -Net	57	99	151	256	361	466	571
DPA-Net	9310	9310	9310	9310	9310	9310	9310
SCSNet	497	497	497	497	497	497	497
CSNet ⁺	381	423	475	579	685	789	895
ISTA-Net ⁺	176	259	293	433	572	712	852
ISTA-Net ⁺⁺	760	760	760	760	760	760	760
COAST	1122	1122	1122	1122	1122	1122	1122
OPINE-Net	205	231	258	287	349	402	414
CSRN	132	143	156	193	231	268	306

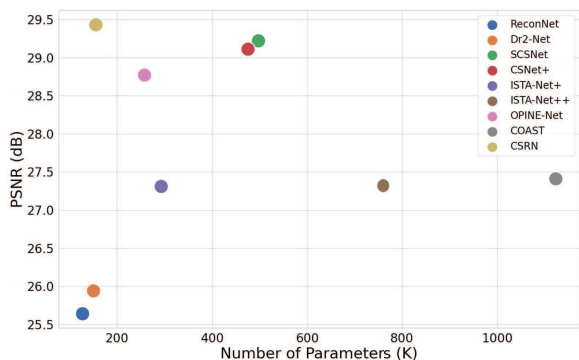


Fig. 10: Comparison of the PSNRs and parameters of different deep learning-based methods on Set14 for a sample ratio of 0.1.

fact that stacking too many basic reconstruction blocks at high sample ratios makes gradient propagation difficult during training. In general, the results demonstrate that progressive initial reconstruction achieves a competitive reconstruction quality when it comes to reconstructing initial images with a smaller number of parameters.

E. Analysis of RRFM

The RRFM is characterized by multi-scale feature learning and a recurrent structure; it can recurrently process input features through a residual block and fuse the features of different receptive fields. To investigate the effect of the two parts of the RRFM, we remove the recurrent connection from the RRFM and the convolutional layer at the end of the RRFM, and thus, the RRFM is reduced to a normal residual block (RB). We compare the reconstruction qualities of CSRN with the RRFM and RB on Set5 and Set11, and the results are given in Fig. 11. As shown, without the feature fusion operation and recurrent connection, the reconstruction quality of CSRN obviously decreases. This suggests that the feature fusion operation conducted using 1*1 convolution is helpful for the comprehensive utilization of the multi-scale feature maps generated during recurrences. Additionally, this means that the recurrent connection can enhance the network’s ability to explore the useful information in feature maps.

Thanks to the recurrent structure of the RRFM, the number of parameters is reduced and the cost of training the neural

TABLE V: Comparison of the Parameters Needed for Simple Initial Reconstruction and Progressive Initial Reconstruction

Sample ratio	Simple initial reconstruction (K)	Progressive initial reconstruction (K)
0.01	10.2	13.9
0.05	52.2	24.4
0.1	104.4	37.5
0.2	208.9	75
0.3	313.3	112.5
0.4	417.8	150
0.5	522.2	187.6

TABLE VI: Reconstruction Quality Comparison of Simple Initial Reconstruction and Progressive Initial Reconstruction

Sample ratio	Simple initial reconstruction (dB)	Progressive initial reconstruction (dB)
0.01	24.53	24.74
0.05	28.14	28.31
0.1	30.19	30.28
0.2	32.92	33.01
0.3	35.19	35.22
0.4	37.21	37.23
0.5	39.33	39.22

network model is thus alleviated. It is also worth noting that although the performance of CSRN with the RB is not as good as that of CSRN with the RRFM, it is still comparable to CSNet⁺. This demonstrates the effectiveness of the overall structural design of CSRN. Due to the absence of the recurrent structure, the computational requirements of CSRN with the RB decrease, and thus it can recover images with a smaller memory footprint compared to normal CSRN. When limited computing resources are available, we can use CSRN with the RB to recover images with a relatively good quality.

F. Analysis of Feature Compression Strategy

In this subsection, we investigate the effect of the feature compression strategy on the network performance in terms of the reconstruction quality, generality and resource consumption of the model.

To test the effect of the compression strategy on the reconstruction quality, we replace $Conv(m, 2, 2)$ at the head of the residual reconstruction sub-network with $Conv(m, 3, 1)$, and thus the feature maps will retain the resolution of the original image during the inference process. We denote this model as CSRN-O and compare its performance with CSRN on the Set5 and Set11. As shown in Fig. 12, CSRN can achieve a performance comparable to that of CSRN-O. As the sample ratio further increases, CSRN-O performs better. This can be explained by the fact that in the case of a low sample ratio, some information contained in the feature maps F_i from the initial reconstruction sub-network is redundant for residual image reconstruction, and thus compressing the feature maps helps the network to extract meaningful information. As the sample ratio further increases, more information can be preserved during the sampling process, and F_i can contain more useful information for residual images. In this case, the compression operation may cause some information loss and

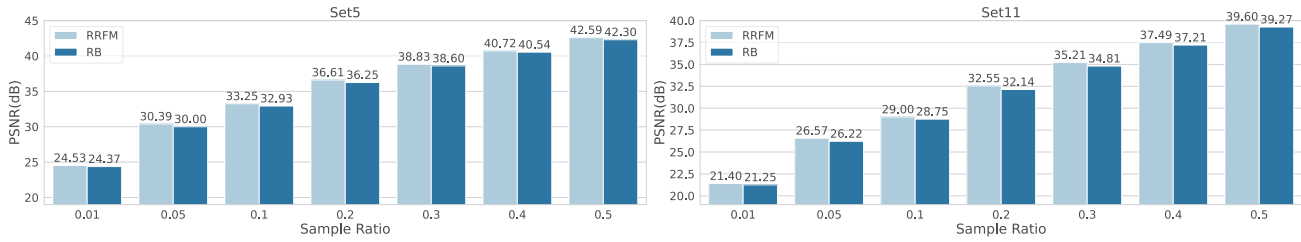


Fig. 11: Reconstruction quality comparison of the RRFM and RB.

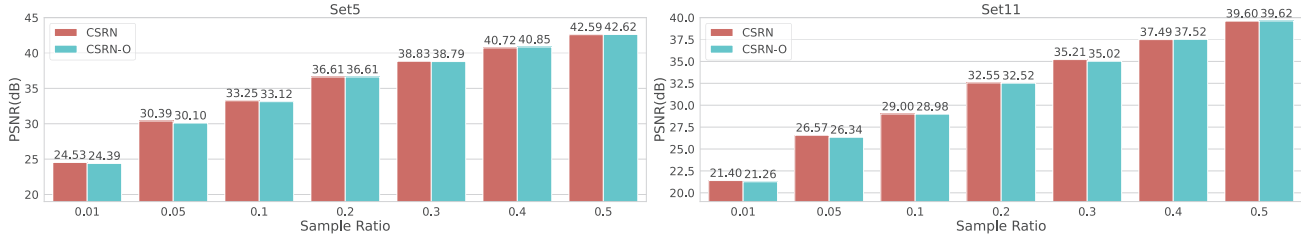


Fig. 12: Reconstruction quality comparison of CSRN and CSRN-O.

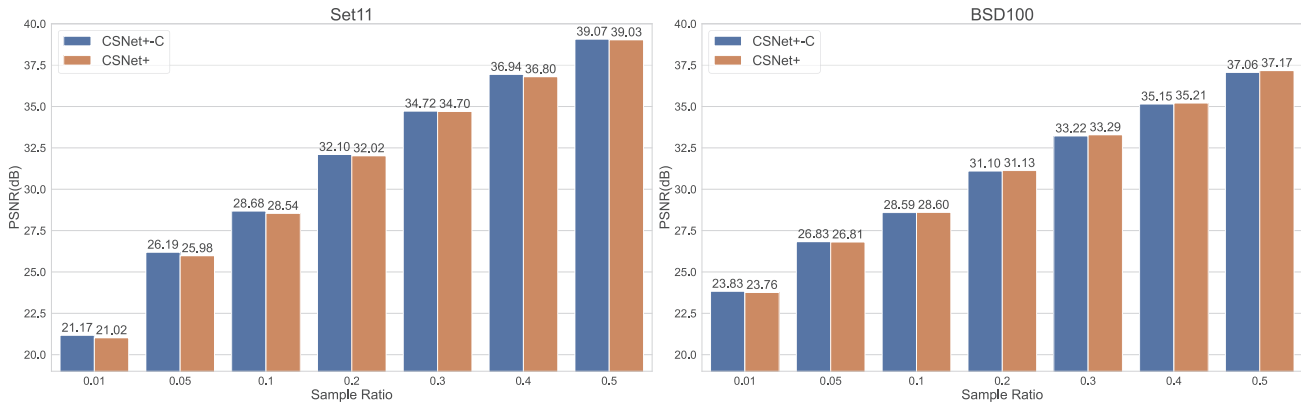


Fig. 13: Reconstruction quality comparison of CSNet⁺ and CSNet⁺-C.

CSRN’s performance may decrease slightly. As we only use a relatively simple strategy for compression, a better-designed method may be able to eliminate such information loss.

To verify the generality of the compression strategy, we apply it to CSNet⁺ by replacing $Conv(64, 3, 1)$ at the head of the deep reconstruction part with $Conv(64, 2, 2)$, and we replace $Conv(64, 3, 1)$ at the tail of the deep reconstruction part with $PixelShuffle(2)$ and $Conv(16, 3, 1)$. We denote CSNet⁺ with the compression strategy as CSNet⁺-C and compare it with the original CSNet⁺. The results are shown in Fig. 13; it can be seen that like CSRN, CSNet⁺-C can achieve a better reconstruction quality at low sample ratios. As the sample ratio increases, the reconstruction quality of CSNet⁺ approaches that of CSNet⁺-C and finally surpasses that of CSNet⁺-C. Therefore, CSNet⁺-C can achieve a reconstruction quality that is comparable to that of CSNet⁺, which proves that the feature compression strategy has a certain degree of generalizability.

We test the memory consumption during the feedforward process and the reconstruction speed to explore the effect of the compression strategy on the model’s resource consump-

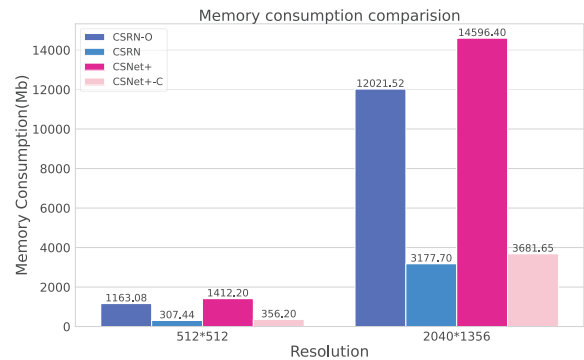


Fig. 14: Comparison of the effects of the compression strategy on memory consumption.

tion. We send images with resolutions of 512×512 and 2040×1356 into the abovementioned models to test their memory consumption, and the results are shown in Fig. 14. As expected, the compression strategy reduces the size of the feature maps, and thus it can significantly reduce the

memory consumption, especially when high-resolution images are utilized.

G. Summary of the Three Proposed Strategies

We have independently analyzed the three strategies proposed in this paper, which include the RRFM, progressive initial reconstruction and feature compression strategy. In this subsection, we will summarize the advantages of each strategy. The feature compression strategy reduces the size of the feature map to one fourth of the size of the original map, and this reduces the number of parameters and decreases the memory consumption even more than progressive initial reconstruction. The RRFM is the most important part of our model; it significantly reduces reconstruction errors by using residual reconstruction to preserve reconstruction details.

V. CONCLUSION

In this paper, we propose a sustainable image compressed sensing method that can be directly used for image sampling and recovery. The method is both lightweight and efficient, and it can achieve a better performance with less memory consumption, a smaller number of parameters and competitive reconstruction time. Recently, neural networks with physics-driven structures for image compressed sensing have attracted more attention. These networks unfold optimization steps using neural networks, which enables some prior knowledge to be implicitly contained in the model. As a result, these networks have achieved a certain degree of interpretability and thus have the potential to be used in our future research.

REFERENCES

- [1] D. Donoho, "Compressed sensing," *IEEE Transactions on Information Theory*, vol. 52, no. 4, pp. 1289–1306, 2006.
- [2] F. Rousset, N. Ducros, A. Farina, G. Valentini, C. D'Andrea, and F. Peyrin, "Adaptive basis scan by wavelet prediction for single-pixel imaging," *IEEE Transactions on Computational Imaging*, vol. 3, no. 1, pp. 36–46, 2017.
- [3] T. Küstner, C. Würslin, S. Gatidis, P. Martirosian, K. Nikolaou, N. Schwenzer, F. Schick, B. Yang, and H. Schmidt, "MR image reconstruction using a combination of compressed sensing and partial Fourier acquisition: ESPReSSo," *IEEE Transactions on Medical Imaging*.
- [4] L. Gan, "Block compressed sensing of natural images," in *2007 15th International Conference on Digital Signal Processing*, 2007, pp. 403–406.
- [5] Y. Kim, M. S. Nadar, and A. Bilgin, "Compressed sensing using a Gaussian scale mixtures model in wavelet domain," in *2010 IEEE International Conference on Image Processing*, 2010, pp. 3365–3368.
- [6] S. Mun and J. E. Fowler, "Block compressed sensing of images using directional transforms," in *2010 Data Compression Conference*, 2010, pp. 547–547.
- [7] J. Zhang, D. Zhao, and W. Gao, "Group-based sparse representation for image restoration," *IEEE Transactions on Image Processing*, vol. 23, no. 8, pp. 3336–3351, 2014.
- [8] C. Zhao, S. Ma, J. Zhang, R. Xiong, and W. Gao, "Video compressive sensing reconstruction via reweighted residual sparsity," *IEEE Transactions on Circuits and Systems for Video Technology*, vol. 27, no. 6, pp. 1182–1195, 2017.
- [9] M. Azghani, M. Karimi, and F. Marvasti, "Multihypothesis compressed video sensing technique," *IEEE Transactions on Circuits and Systems for Video Technology*, vol. 26, no. 4, pp. 627–635, 2016.
- [10] Y. Liu, M. Li, and D. A. Pados, "Motion-aware decoding of compressed-sensed video," *IEEE Transactions on Circuits and Systems for Video Technology*, vol. 23, no. 3, pp. 438–444, 2013.
- [11] A. Krizhevsky, I. Sutskever, and G. E. Hinton, "ImageNet classification with deep convolutional neural networks," in *Proceedings of the 25th International Conference on Neural Information Processing Systems – Volume 1*, ser. NIPS'12. Red Hook, NY, USA: Curran Associates Inc., 2012, p. 1097–1105.
- [12] C. Dong, C. C. Loy, K. He, and X. Tang, "Image super-resolution using deep convolutional networks," *IEEE Transactions on Pattern Analysis and Machine Intelligence*, vol. 38, no. 2, pp. 295–307, 2016.
- [13] A. Lahiri, S. Bairagya, S. Bera, S. Haldar, and P. K. Biswas, "Lightweight modules for efficient deep learning based image restoration," *IEEE Transactions on Circuits and Systems for Video Technology*, vol. 31, no. 4, pp. 1395–1410, 2021.
- [14] W. Shi, S. Liu, F. Jiang, and D. Zhao, "Video compressed sensing using a convolutional neural network," *IEEE Transactions on Circuits and Systems for Video Technology*, vol. 31, no. 2, pp. 425–438, 2021.
- [15] G. Yang, S. Yu, H. Dong, G. Slabaugh, P. L. Dragotti, X. Ye, F. Liu, S. Arridge, J. Keegan, Y. Guo, and D. Firmin, "DAGAN: Deep de-aliasing generative adversarial networks for fast compressed sensing MRI reconstruction," *IEEE Transactions on Medical Imaging*, vol. 37, no. 6, pp. 1310–1321, 2018.
- [16] C. Ma, J. T. Zhou, X. Zhang, and Y. Zhou, "Deep unfolding for compressed sensing with denoiser," in *2022 IEEE International Conference on Multimedia and Expo (ICME)*. IEEE, 2022, pp. 01–06.
- [17] G. J. van Wyk and A. S. Bosman, "Evolutionary neural architecture search for image restoration," in *2019 International Joint Conference on Neural Networks (IJCNN)*. IEEE, 2019, pp. 1–8.
- [18] Y. Yang, H. Li, S. You, F. Wang, C. Qian, and Z. Lin, "ISTA-NAS: Efficient and consistent neural architecture search by sparse coding," *Advances in Neural Information Processing Systems*, vol. 33, pp. 10503–10513, 2020.
- [19] B. Zhou and S. K. Zhou, "DuDoRNet: Learning a dual-domain recurrent network for fast MRI reconstruction with deep T1 prior," in *Proceedings of the IEEE/CVF Conference on Computer Vision and Pattern Recognition*, 2020, pp. 4273–4282.
- [20] J. Ni, F. Zhang, Q. Yin, Y. Zhou, H.-C. Li, and W. Hong, "Random neighbor pixel-block-based deep recurrent learning for polarimetric SAR image classification," *IEEE Transactions on Geoscience and Remote Sensing*, vol. 59, no. 9, pp. 7557–7569, 2020.
- [21] A. Adler, D. Boubllil, and M. Zibulevsky, "Block-based compressed sensing of images via deep learning," in *2017 IEEE 19th International Workshop on Multimedia Signal Processing (MMSp)*. IEEE, 2017, pp. 1–6.
- [22] G. N. K. Reddy, M. S. Manikandan, and N. N. Murty, "Lightweight compressed sensing (CS) and partial DCT based compression schemes for energy-efficient wearable PPG monitoring devices," in *2021 IEEE International Conference on Health, Instrumentation & Measurement, and Natural Sciences (InHeNce)*. IEEE, 2021, pp. 1–6.
- [23] A. Mousavi, A. B. Patel, and R. G. Baraniuk, "A deep learning approach to structured signal recovery," in *2015 53rd Annual Allerton Conference on Communication, Control, and Computing (Allerton)*, 2015, pp. 1336–1343.
- [24] K. Kulkarni, S. Lohit, P. Turaga, R. Kerviche, and A. Ashok, "ReconNet: Non-iterative reconstruction of images from compressively sensed measurements," in *2016 IEEE Conference on Computer Vision and Pattern Recognition (CVPR)*, 2016, pp. 449–458.
- [25] H. Yao, F. Dai, S. Zhang, Y. Zhang, Q. Tian, and C. Xu, "Dr2-Net: Deep residual reconstruction network for image compressive sensing," *Neurocomputing*, vol. 359, pp. 483–493, 2019.
- [26] Y. Sun, J. Chen, Q. Liu, B. Liu, and G. Guo, "Dual-path attention network for compressed sensing image reconstruction," *IEEE Transactions on Image Processing*, vol. 29, pp. 9482–9495, 2020.
- [27] W. Shi, F. Jiang, S. Zhang, and D. Zhao, "Deep networks for compressed image sensing," in *2017 IEEE International Conference on Multimedia and Expo (ICME)*, 2017, pp. 877–882.
- [28] J. Zhang and B. Ghanem, "ISTA-Net: Interpretable optimization-inspired deep network for image compressive sensing," in *2018 IEEE/CVF Conference on Computer Vision and Pattern Recognition*, 2018, pp. 1828–1837.
- [29] Z. Zhang, Y. Liu, J. Liu, F. Wen, and C. Zhu, "AMP-Net: Denoising-based deep unfolding for compressive image sensing," *IEEE Transactions on Image Processing*, vol. 30, pp. 1487–1500, 2021.
- [30] D. You, J. Zhang, J. Xie, B. Chen, and S. Ma, "COAST: Controllable Arbitrary-Sampling neTwork for compressive sensing," *IEEE Transactions on Image Processing*, vol. 30, pp. 6066–6080, 2021.
- [31] W. Shi, J. Caballero, F. Huszár, J. Totz, A. P. Aitken, R. Bishop, D. Rueckert, and Z. Wang, "Real-time single image and video super-resolution using an efficient sub-pixel convolutional neural network," in

2016 IEEE Conference on Computer Vision and Pattern Recognition (CVPR), 2016, pp. 1874–1883.

- [32] W. Shi, F. Jiang, S. Liu, and D. Zhao, “Image compressed sensing using convolutional neural network,” *IEEE Transactions on Image Processing*, vol. 29, pp. 375–388, 2020.
- [33] K. He, X. Zhang, S. Ren, and J. Sun, “Deep residual learning for image recognition,” in *2016 IEEE Conference on Computer Vision and Pattern Recognition (CVPR)*, 2016, pp. 770–778.
- [34] B. Lim, S. Son, H. Kim, S. Nah, and K. M. Lee, “Enhanced deep residual networks for single image super-resolution,” in *2017 IEEE Conference on Computer Vision and Pattern Recognition Workshops (CVPRW)*, 2017, pp. 1132–1140.
- [35] J. Zhang, C. Zhao, and W. Gao, “Optimization-inspired compact deep compressive sensing,” *IEEE Journal of Selected Topics in Signal Processing*, vol. 14, no. 4, pp. 765–774, 2020.
- [36] J. Kim, J. K. Lee, and K. M. Lee, “Accurate image super-resolution using very deep convolutional networks,” in *2016 IEEE Conference on Computer Vision and Pattern Recognition (CVPR)*, 2016, pp. 1646–1654.
- [37] M. Bevilacqua, A. Roumy, C. Guillemot, and M.-L. Alberi Morel, “Low-complexity single-image super-resolution based on nonnegative neighbor embedding,” in *British Machine Vision Conference (BMVC)*, Guildford, Surrey, United Kingdom, Sep. 2012.
- [38] R. Zeyde, M. Elad, and M. Protter, “On single image scale-up using sparse-representations,” in *Curves and Surfaces*, J.-D. Boissonnat, P. Chenin, A. Cohen, C. Gout, T. Lyche, M.-L. Mazure, and L. Schumaker, Eds. Berlin, Heidelberg: Springer Berlin Heidelberg, 2012, pp. 711–730.
- [39] D. Martin, C. Fowlkes, D. Tal, and J. Malik, “A database of human segmented natural images and its application to evaluating segmentation algorithms and measuring ecological statistics,” in *Proceedings of the Eighth IEEE International Conference on Computer Vision (ICCV 2001)*, vol. 2, 2001, pp. 416–423 vol.2.
- [40] J.-B. Huang, A. Singh, and N. Ahuja, “Single image super-resolution from transformed self-exemplars,” in *2015 IEEE Conference on Computer Vision and Pattern Recognition (CVPR)*, 2015, pp. 5197–5206.
- [41] R. Timofte, E. Agustsson, L. V. Gool, M.-H. Yang, L. Zhang, B. Lim, S. Son, H. Kim, S. Nah, K. M. Lee, X. Wang, Y. Tian, K. Yu, Y. Zhang, S. Wu, C. Dong, L. Lin, Y. Qiao, C. C. Loy, W. Bae, J. Yoo, Y. Han, J. C. Ye, J.-S. Choi, M. Kim, Y. Fan, J. Yu, W. Han, D. Liu, H. Yu, Z. Wang, H. Shi, X. Wang, T. S. Huang, Y. Chen, K. Zhang, W. Zuo, Z. Tang, L. Luo, S. Li, M. Fu, L. Cao, W. Heng, G. Bui, T. Le, Y. Duan, D. Tao, R. Wang, X. Lin, J. Pang, J. Xu, Y. Zhao, X. Xu, J. Pan, D. Sun, Y. Zhang, X. Song, Y. Dai, X. Qin, X.-P. Huynh, T. Guo, H. S. Mousavi, T. H. Vu, V. Monga, C. Cruz, K. Egiazarian, V. Katkovnik, R. Mehta, A. K. Jain, A. Agarwalla, C. V. S. Praveen, R. Zhou, H. Wen, C. Zhu, Z. Xia, Z. Wang, and Q. Guo, “NTIRE 2017 challenge on single image super-resolution: Methods and results,” in *2017 IEEE Conference on Computer Vision and Pattern Recognition Workshops (CVPRW)*, 2017, pp. 1110–1121.
- [42] A. Hore and D. Ziou, “Image quality metrics: PSNR vs. SSIM,” in *2010 20th International Conference on Pattern Recognition*. IEEE, 2010, pp. 2366–2369.
- [43] Z. Wang, A. C. Bovik, H. R. Sheikh, and E. P. Simoncelli, “Image quality assessment: From error visibility to structural similarity,” *IEEE Transactions on Image Processing*, vol. 13, no. 4, pp. 600–612, 2004.
- [44] Z. Zhao, X. Xie, C. Wang, S. Mao, W. Liu, and G. Shi, “ROI-CSNet: Compressive sensing network for ROI-aware image recovery,” *Signal Processing: Image Communication*, vol. 78, pp. 113–124, 2019.
- [45] M. Yamac, U. Akpinar, E. Sahin, S. Kiranyaz, and M. Gabbouj, “Generalized tensor summation compressive sensing network (GTSNET): An easy to learn compressive sensing operation,” *arXiv preprint arXiv:2108.03167*, 2021.
- [46] C. Chen, E. W. Tramel, and J. E. Fowler, “Compressed-sensing recovery of images and video using multihypothesis predictions,” in *2011 Conference Record of the Forty-Fifth Asilomar Conference on Signals, Systems and Computers (ASILOMAR)*, 2011, pp. 1193–1198.
- [47] W. Shi, F. Jiang, S. Liu, and D. Zhao, “Scalable convolutional neural network for image compressed sensing,” in *2019 IEEE/CVF Conference on Computer Vision and Pattern Recognition (CVPR)*, 2019, pp. 12282–12291.
- [48] D. You, J. Xie, and J. Zhang, “ISTA-NET++: Flexible deep unfolding network for compressive sensing,” in *2021 IEEE International Conference on Multimedia and Expo (ICME)*, 2021, pp. 1–6.



is an IEEE member.

Yu Zhou received the B.Sc. degree in electronics and information engineering and the M.Sc. degree in circuits and systems from Xidian University, Xi’an, China, in 2009 and 2012, respectively, and the Ph.D. degree in computer science from the City University of Hong Kong, Hong Kong, in 2017. He is currently an Assistant Professor with College of Computer Science and Software Engineering, Shenzhen University, Shenzhen, China. His current research interests include computational intelligence, machine learning and intelligent information processing. He



Yu Chen received the B.Eng. degree from East China University of Technology, JiangXi, China, in 2020. He is currently pursuing the M.Sc. degree at the College of Computer Science and Software Engineering, Shenzhen University, Shenzhen, China. His current research areas are compressed sensing and machine learning.



Nationalities, China. His research interests include algorithms design and analysis, combinatorial optimization, wireless and UAV networking.

Xiao Zhang received the B.Eng. and M.Eng. degrees from South-Central University for Nationalities, Wuhan, China, in 2009 and 2011 respectively. In 2015, he was a visiting scholar with the Utah State University, Utah, USA. He received his Ph.D. degree from Department of Computer Science in City University of Hong Kong, Hong Kong, 2016. During 2016-2019, he was a postdoc research fellow at Singapore University of Technology and Design. Currently, he is Associate Professor with College of Computer Science, South-Central University for



Pan Lai received the Ph.D. degree from the School of Computer Engineering, Nanyang Technological University, in 2016. He is currently an Associate Professor with South-Central University for Nationalities, China. He was a Post-Doctoral Research Fellow with the Singapore University of Technology and Design, Singapore, from 2016 to 2019. His research interests include resource allocation and scheduling algorithm design in computer and network systems, network economics, and game theory.



Lei Huang (Senior Member, IEEE) received the B.Sc. and Ph.D. degrees in electronic engineering from Xidian University, Xi'an, China, in 2000 and 2005, respectively. Since 2014, he has been with the College of Electronics and Information Engineering, Shenzhen University, where he is currently a Distinguished Professor and the Director of the Shenzhen Key Laboratory of Advanced Navigation Technology. He has undertaken eight projects from the National Natural Science Foundation of China (NSFC), including the National Science Funds for

Distinguished Young Scholar. His research interests include array signal processing, statistical signal processing, sparse signal processing, and their applications in radar, navigation, and wireless communications. In 2018, he was elected as a fellow of IET. Since 2016, he has been an Elected Member of the Sensor Array and Multichannel (SAM) Technical Committee of the IEEE Signal Processing Society. He has been serving as an Associate Editor for the IEEE TRANSACTIONS ON SIGNAL PROCESSING since 2015. He is currently a Senior Area Editor of the IEEE TRANSACTIONS ON SIGNAL PROCESSING.



Jianmin Jiang received PhD from the University of Nottingham, UK, in 1994. From 1997 to 2001, he worked as a full professor of Computing at the University of Glamorgan, Wales, UK. In 2002, he joined the University of Bradford, UK, as a Chair Professor of Digital Media, and Director of Digital Media Systems Research Institute. He worked at the University of Surrey, UK, as a full professor during 2010-2015 and a distinguished chair professor (1000-plan) at Tianjin University, China, during 2010-2013. He is currently a Distinguished Chair

Professor and director of the Research Institute for Future Media Computing at the College of Computer Science Software Engineering, Shenzhen University, China. He was a chartered engineer, fellow of IEE(IET), fellow of RSA, member of EPSRC College in the UK, and EU FP-6/7 evaluator. His research interests is primarily focused on deep learning applications in multimedia content understanding and analysis, brain perceived pattern recognition and intelligent image/video processing. He has published around 400 refereed research papers in international leading journals and conferences.